High-Performance Rapid MR Parameter Mapping Using Model-Based Deep Adversarial Learning

Fang Liu, Ph.D.[1,*], **Richard Kijowski, M.D.**[2], **Li Feng, Ph.D.**[3], **Georges El Fakhri, Ph.D.**[1]

[1]Department of Radiology, Massachusetts General Hospital, Harvard Medical School, Boston, Massachusetts, USA

[2]Department of Radiology, University of Wisconsin-Madison, Madison, Wisconsin, USA

[3]Biomedical Engineering and Imaging Institute, Icahn School of Medicine at Mount Sinai, New York, USA

Abstract

Purpose: To develop and evaluate a deep adversarial learning-based image reconstruction approach for rapid and efficient MR parameter mapping.

Methods: The proposed method provides an image reconstruction framework by combining the end-to-end convolutional neural network (CNN) mapping, adversarial learning, and MR physical models. The CNN performs direct image-to-parameter mapping by transforming a series of undersampled images directly into MR parameter maps. Adversarial learning is used to improve image sharpness and enable better texture restoration during the image-to-parameter conversion. An additional pathway concerning the MR signal model is added between the estimated parameter maps and undersampled k-space data to ensure the data consistency during network training. The proposed framework was evaluated on T_2 mapping of the brain and the knee at an acceleration rate R=8 and was compared with other state-of-the-art reconstruction methods. Global and regional quantitative assessments were performed to demonstrate the reconstruction performance of the proposed method.

Results: The proposed adversarial learning approach achieved accurate T_2 mapping up to R=8 in brain and knee joint image datasets. Compared to conventional reconstruction approaches that

---

*Corresponding Author: Fang Liu, Ph.D., Gordon Center for Medical Imaging, Massachusetts General Hospital, Harvard Medical School, 125 Nashua Street, 6th floor, Suite 660, Boston, Massachusetts 02114, Phone: 617-643-1961, fliu12@mgh.harvard.edu.

exploit image sparsity and low-rankness, the proposed method yielded lower errors and higher similarity to the reference and better image sharpness in the T_2 estimation. The quantitative metrics were normalized root mean square error of 3.6% for brain and 7.3% for knee, structural similarity index of 85.1% for brain and 83.2% for knee, and tenengrad measures of 9.2% for brain and 10.1% for the knee. The adversarial approach also achieved better performance for maintaining greater image texture and sharpness in comparison to the CNN approach without adversarial learning.

Conclusion: The proposed framework by incorporating the efficient end-to-end CNN mapping, adversarial learning, and physical model enforced data consistency is a promising approach for rapid and efficient reconstruction of quantitative MR parameters.

Keywords

Deep Learning; MR Parameter Mapping; Convolutional Neural Network; Model-based Reconstruction; Generative Adversarial Network; Adversarial Learning

INTRODUCTION

Quantitative MR parameter mapping has been shown as valuable image biomarkers for assessing a variety of diseases(1). Traditional approaches for imaging MR parameters such as the spin-spin relaxation time (T_2) usually require repeated acquisitions to capture a set of imaging contrast, followed by a pixel-wise curve fitting using an MR signal model. This leads to longer scan times compared to conventional contrast-weighted imaging and thus limits its widespread clinical use. As a result, the acceleration for parameter mapping has become a popular research direction in the MR research community.

There has been recent interest in using deep learning to accelerate MR acquisition and reconstruction (2–10). We have previously developed a deep learning reconstruction method, called Model-Augmented Neural neTwork with Incoherence Sampling (MANTIS) (11), for mapping T_2 parameters using a rapid multi-echo spin-echo acquisition. MANTIS uses an efficient end-to-end CNN mapping (modified U-Net (12)) to directly convert a series of undersampled images into parametric maps (e.g., a T_2 map and a proton density map I_0 for T_2 mapping) by exploiting the spatial-temporal information in undersampled images. In addition, a physical model characterizing the MR signal evolution is further incorporated into the learning framework to guide the image-to-parameter transform, so that the parameter maps can be robustly estimated directly from undersampled images.

A number of studies have also shown that when training a deep learning model for imaging applications, the implementation of a simple l_1/l_2-norm as a training loss could result in image blurring and loss of image details (13). This is also a potential challenge for the MANTIS framework. While MANTIS has demonstrated promising results for accelerated T_2 mapping, the use of a simple training loss could limit the further acceleration of T_2 mapping, particularly at high image resolution. Our study and others have recently demonstrated that the Generative Adversarial Network (GAN) (14) can improve image sharpness and better preserve image texture through the addition of an adversarial training process into deep learning-based MR reconstruction (15–18). The aim of this current study

was thus to expand the MANTIS framework by incorporating adversarial training for improved reconstruction performance. The feasibility of this new framework, referred to as MANTIS-GAN, was evaluated for T_2 mapping in simulated brain imaging datasets and real knee imaging datasets.

THEORY

This section describes the extension of MANTIS to MANTIS-GAN tailored for T_2 mapping based on a single exponential decay model. This new framework could also be applied for mapping other MR parameters with corresponding MR signal models.

MANTIS: Deep Learning-based Parameter Mapping with Model-Consistency

In the setup for T_2 mapping, the jth echo image can be reconstructed from a subset of k-space measurements as:

$$d_j = Ei_j + \varepsilon \qquad [1]$$

where the d_j is the undersampled k-space data, i_j is the to-be-reconstructed image with an image size of $n_x \times n_y$, ε represents the complex Gaussian noise (19). E is the encoding matrix, which can be further expanded as:

$$E = MF \qquad [2]$$

Here, F is an encoding operator for fast Fourier Transform and M is an undersampling mask to selectively acquire k-space locations. The signal evolution for T_2 mapping follows the exponential decay at the jth echo (TE_j) as:

$$i_j = S_j(I_0, T_2) = I_0 \cdot e^{-TE_j/T_2} \qquad [3]$$

where I_0 and T_2 is the proton density and spin-spin relaxation time, respectively. A model-based reconstruction scheme, by incorporating Eq [3] into Eq. [1], can be formulated as:

$$\tilde{I}_0, \widetilde{T}_2 = \arg \min_{I_0, T_2} \sum_{j=1}^{t} \| ES_j(I_0, T_2) - d_j \|_2^2 \qquad [4]$$

where $\|\cdot\|_2$ denotes the l_2 norm and t is the number of acquired echoes.

Inspired by the model-based reconstruction, the original MANTIS framework reformulates the Eq[4] into a network training loss. As shown in Figure 1, an end-to-end mapping CNN $G(i_u \mid \theta): i_u \rightarrow (\tilde{I}_0, \widetilde{T}_2)$ with network parameters θ is designated to directly convert undersampled images into the parameter maps through domain transform learning. This first loss term (loss 1 in the figure) ensures the fact that the mapping CNN can output parameter maps that, by following the MR physics, can produce undersampled k-space data consistent with the acquired k-space measurements. In addition, the standard supervised learning can be treated as a strong regularizer, where the second loss term (loss 2 in the figure) provides that the mapping CNN generates similar parametric maps to the reference parameter maps in

the sense of l_2 norm. Overall, this optimization problem is then reformulated to minimize a training loss as:

$$L_{cyc}(G) = \lambda_1 \mathbb{E}_{i_u - P(i_u)} \left[\sum_{j=1}^{t} \| ES_j(G(i_u \mid \theta)) - d_j \|_2^2 \right]$$
$$+ \lambda_2 \mathbb{E}_{i_u \sim P(i_u)} [\| G(i_u \mid \theta) - (I_0, T_2) \|_2]$$

[5]

Where λ_1 and λ_2 are weight factors to balance two loss terms, respectively, assuming that there are training image datasets including reference parameter maps (I_0, T_2) and the corresponding undersampled images i_u which can be obtained by using zero-filling reconstruction with a pre-defined undersampling mask M on the fully-sampled images i. $\mathbb{E}_{i_u \sim P(i_u)}[\cdot]$ is an expectation operator given the training sample i_u belongs to the data distribution $P i(_u)$ of the undersampled image datasets.

Adversarial Loss

While these two l_2 norm loss terms can ensure favorable reconstruction by removing noise and artifacts, recent studies have found that sole use of pixel-wise loss terms such as l_1 or l_2 norm can result in image blurring and loss of image texture (11,15–18). To alleviate this problem, GAN has been recently introduced to enforce image sharpness and texture preservation, as shown in several image restoration applications(15–18). More specifically, GAN uses a CNN discriminator to assess the similarity between the output of CNN mapping and the references. An adversarial loss can then be implemented into the training framework as a third loss term in Figure 1. The adversarial loss can capture multiple-level local and global features so it can better represent image texture and pattern than the simple loss does. Mathematically, a multiple-layer CNN discriminator $D((I_0,T_2) \mid \delta) : (I_0,T_2) \rightarrow 1$ with network parameters δ is designed to distinguish reconstructed parameter maps versus reference parameter maps from the data distribution $P(I_0,T_2)$ of the reference map datasets. This discriminator D outputs a probability value to measure how likely the estimated $(\tilde{I}_0, \tilde{T}_2)$ comes from the reference map datasets. The adversarial loss can be formatted as:

$$L_{gan}(G, D) = \mathbb{E}_{(I_0, T_2) \sim P(I_0, T_2)} [\log D((I_0, T_2) \mid \delta)]$$
$$+ \mathbb{E}_{i_u \sim P(i_u)} [\log(1 - D(G(i_u \mid \theta) \mid \delta))]$$

[6]

MANTIS-GAN: MANTIS with Adversarial Network

By combining all three loss terms, a full loss function can be written as:

$$L_{full} = L_{cyc} + L_{gan} = \lambda_1 \mathbb{E}_{i_u \sim P(i_u)} \left[\sum_{j=1}^{t} \| ES_j(G(i_u \mid \theta)) - d_j \|_2^2 \right]$$
$$+ \lambda_2 \mathbb{E}_{i_u \sim P(i_u)} [\| G(i_u \mid \theta) - (I_0, T_2) \|_2] + \lambda_3$$
$$\left(\mathbb{E}_{(I_0, T_2) \sim P(I_0, T_2)} [\log D((I_0, T_2) \mid \delta)] + \mathbb{E}_{i_u \sim P(i_u)} [\log(1 - D(G(i_u \mid \theta) \mid \delta))] \right)$$

[7]

Here λ_3 is a weight factor in balancing the GAN effect on the overall reconstruction. The full loss function can then be optimized in the training step using a two-player minimax game(14) as:

$$\widehat{G}, \widehat{D} = \arg\min_{G} \max_{D} L_{full}(G, D) \tag{8}$$

where G aims to minimize this loss function against the adversary D that seeks to maximize it. With successful training, the GAN theory ensures that this competing scheme can result in an optimal $G(i_u \mid \theta): i_u \rightarrow (\widetilde{I}_0, \widetilde{T}_2)$ to generate parameter maps indistinguishable from the real reference maps based on the judgment of the discriminator D. Once the training is completed and satisfied, the CNN mapping can be fixed and directly applied to convert newly undersampled images into parameter maps for the reconstruction.

METHODS

Image Datasets

Simulated Brain Data—Twenty digital brain models made from 20 healthy adults with intersubject anatomical variabilities were obtained from the BrainWeb project (https://brainweb.bic.mni.mcgill.ca/). Each brain model was acquired by registering and averaging four whole-head high-resolution isotropic (1 mm^3) T$_1$-, T$_2$-, and I$_0$-weighted MRI scans from each subject. A 3D tissue mask covering the whole head for eleven tissue types including gray matter, white matter, cerebrospinal fluid was created by classifying the voxel intensities from all MR images using a fuzzy minimum distance classification algorithm(20). These models provided realistic brain structural features that were ideal for generating image datasets with brain anatomical information. Different tissue relaxation parameters, including T$_1$,T$_2$ and I$_0$, were assigned to each tissue type based on previous literature values (21,22). The synthetic image data were generated using our MRiLab (23) simulation system on the brain models. The MRiLab (https://leoliuf.github.io/MRiLab/) is an open-source Bloch-simulation system, which is capable of simulating MR formulation for various pulse sequences given radiofrequency (RF) pulses, gradient waveforms, and acquisition schemes. After loading the digital model, a virtual MRI scan was configured to specify the pulse sequence, which defines time-varying RF pulses and imaging gradients to obtain the desired image contrast, resolution, and acquisition trajectory. The simulation was performed through a discrete-time solution of the Bloch-equation by mean of rotation and exponential scaling matrices at each time throughout the prescribed sequence (23–25). The acquired signal from all voxels in the digital model at the prescribed acquisition windows was then collected to fill the k-space. Upon completion, a fully-sampled image was generated by performing a fast Fourier transform on the k-space data. A schematic description of the simulation workflow is shown in Figure 2. A multi-echo spin-echo T2 mapping sequence was used to simulate axial brain MR images using the following imaging parameters: 16 linear echo times/repetition time (TEs/TR) = [10, 20, 30, …, 160]/2500 ms, flip angle = 90°, slice thickness = 3mm, pixel bandwidth = 488Hz/pixel, number of slices = 40, field of view = 22×22cm^2, and acquired image matrix = 256×256. There was a total of 800 image slices for all subjects.

In-Vivo Knee Data—This retrospective study was performed using T$_2$ mapping images of the knee acquired in 110 symptomatic patients using a 3T GE scanner (Signa Excite Hdx, GE Healthcare, Waukesha, Wisconsin) and an eight-channel phased-array extremity coil (InVivo, Orlando, Florida). The study was approved by the Institutional Review Board and

had a waiver of written informed consent. The imaging parameter for the applied multi-echo spin-echo T_2 mapping sequence includes: 8 echo times/repetition time (TEs/TR) = [7, 16, 25, 34, 43, 52, 62, 71]/1500 ms, flip angle = 90°, slice thickness = 3–3.2mm, pixel bandwidth = 122Hz/pixel, number of slices = 18–20, field of view = 16×16cm^2, acquired image matrix = 320×256, and total scan time = 9min. The images were all acquired in the sagittal plane and were reconstructed on the MR scanner using the vendor-provided method (CartiGram, GE Healthcare, Waukesha, Wisconsin). The reconstructed images were saved as DICOM files after the coil combination and had a mean signal-to-noise ratio (SNR) of ~150 at the first echo image. There was a total of 2107 image slices for all subjects.

Retrospective undersampling was performed to generate the undersampled multi-echo images by multiplying the reference fully sampled *k*-space data with the undersampling masks using a zero-filling reconstruction. An acceleration rate (R)=8 was evaluated for both brain and knee image datasets with an undersampling mask generated using one-dimensional variable-density Cartesian random undersampling patterns (26). The mask had a fully sampled 5% central *k*-space, and the sampling pattern varied for each echo to create temporal incoherence following the compressed sensing strategy. The reference T_2 and I_0 maps were generated by fitting the fully-sampled multi-echo images into the exponential decay model in Eq. [3] using a pixel-wise standard nonlinear least-squares algorithm.

Implementation and Training of the Neural Network

For the end-to-end CNN mapping, a U-Net architecture (12) was adapted from a previous image-to-image translation study (27) into MANTIS and MANTIS-GAN. For the adversarial configuration, a PatchGAN (27) architecture was used for the discriminator network, which aims to differentiate real versus artificial maps using image patch-based assessment in the adversarial process. The choice of such combination is supported by the promising performance of our recent GAN-based architecture in image reconstruction (15). An illustration of the applied U-Net and PatchGAN is shown in Figure 3. The network was coded in Python (Python Software Foundation, Wilmington, Delaware) and used the Keras package (28) running Tensorflow computing backend (29) on a 64-bit Ubuntu Linux system.

The subjects were randomly split into 80%, 10%, and 10% for training, validation, and testing. During the training step, the undersampled images are concatenated from all the echoes together as the input of U-Net. The initialization of network parameters followed the strategy as shown in Ref (30), and an adaptive gradient descent optimization (ADAM) algorithm (31) at a fixed learning rate of 0.0002 was used to update the network parameters. A mini-batch training was performed with each batch consisting of 3 image slices for one iteration. Total iteration steps corresponding to 200 epochs were carried out to ensure convergence of the training (Figure 4), and the best model was determined as the one that had the lowest combined loss 1 + loss 2 value on the validation datasets. A grid search was performed to find the optimal weight factors in the loss function (Eq. [7]). They were λ_1=0.2, λ_2 =1 and λ_3=0.1 for brain images and λ_1=0.1, λ_2 =1 and λ_3=0.01 for knee images in training MANTIS-GAN. MANTIS used the same sets of λ_1 and λ_2 weights to make a fair comparison. All training and evaluation were conducted on a personal computer hosting

an Intel Xeon W3520 CPU, 32 GB global RAM, and one NVidia GTX 1080Ti graphic card which has 3584 CUDA cores and 11GB GPU RAM.

Evaluation of Reconstruction Methods

The reconstruction result of MANTIS-GAN was compared with the state-of-the-art joint x-p (spatial-parametric) reconstruction, including one method using locally low-rank constraint (LLR (32)), and another method using a combined sparsity and low-rank constraint (k-t SLR (33)) on the multiecho image-series. The LLR reconstruction followed the original implementation in Ref (32). The k-t SLR reconstruction followed the default parameter setting using the code in https://research.engineering.uiowa.edu/cbig/content/matlab-codes-k-t-slr, provided by the authors. Because the LLR and k-t SLR provided reconstructed echo images, a T_2 map was then obtained by pixel-wise fitting the reconstructed images into Eq. [3] using a standard nonlinear least-squares algorithm. The MANTIS-GAN was also compared with the original MANTIS without adversarial learning.

Three quantitative metrics focusing on different image aspects were used to assess the global difference between the reconstructed T2 maps and the reference T2 maps. The normalized Root Mean Squared Error (nRMSE) and Structural Similarity (SSIM) index were used to assess the overall reconstruction error and the similarity with respect to the reference, respectively. The relative reduction of Tenengrad measure (34,35) between the reconstructed maps and reference was used to assess the loss of image sharpness. Because this metric is sensitive to the changes of local characteristics of pronounced image edges, a higher Tenengrad value indicates sharper image appearance, thus lower reduction of Tenengrad in contrast to reference indicates better sharpness preservation of the reconstructed maps. Differences of these measures between methods were evaluated using a paired Wilcoxon signed-rank test with statistical significance defined as a p-value less than 0.05.

The regional assessment was performed in the knee images using Region-of-interest (ROI) analysis. The patellar, femoral and tibial cartilage subsections and meniscus of the knee joint were manually segmented by a senior imaging scientist under the supervision of a musculoskeletal radiologist for all testing knee images. The mean T2 values were then obtained from LLR, k-t SLR, MANTIS, and MANTIS-GAN. The agreement between the reconstructed and reference T_2 values were evaluated using the Bland-Altman analysis(36), with a significance level defined as $p{<}0.05$.

RESULTS

Figure 5 shows representative T_2 maps (top row) and proton density I_0 maps (bottom row) estimated from different reconstruction methods, respectively, for testing brain datasets. The LLR reconstruction generated parameter maps with inferior image quality, as indicated by the noticeable artifacts and noises. The k-t SLR outperformed the LLR method as it restored some image details but remained residual artifacts. In contrast, the deep learning-based methods removed most of the artifacts, although the original MANTIS created apparent blurriness at the tissue boundaries due to the high image acceleration. The MANTIS-GAN provided the optimal reconstruction with well-preserved image sharpness, clarity, and tissue texture similar to the reference parameter maps.

Figure 6 demonstrates the comparison of generated T_2 maps from different reconstruction methods for a testing knee dataset. Similar to the example for the brain, there was an observation that MANTIS-GAN provided nearly artifact-free T_2 maps while maintaining better image sharpness and more realistic tissue texture in comparison with the original MANTIS, the LLR and k-t SLR methods.

The qualitative observations in the exemplary figures were further confirmed by the group-wise quantitative analysis, as shown in Table 1, which summarizes the averaged nRMSE, SSIM, and Tenengrad measures between the reference and the reconstructed T_2 maps in all the testing datasets for brain and knee, respectively. In general, The MANTIS and MANTIS-GAN reconstruction outperformed the sparsity and low rankness-based LLR and k-t SLR methods for all metrics with $p<0.001$. Compared with MANTIS, MANTIS-GAN yielded the sharper image appearance (lower Tenengrad: $p<0.001$ for brain, $p=0.03$ for knee) and the higher similarity (higher SSIM: $p=0.01$ for brain, $p=0.01$ for knee) to the reference. Noise suppression was slightly better (lower nRMSE: $p=0.04$ for brain, $p=0.01$ for knee) for MANTIS in contrast to MANTIS-GAN.

The Bland-Altman plots were shown in Figures 7 to compare the reference versus reconstructed T_2 maps in the cartilage subsections and meniscus. In contrast to LLR and k-t SLR, which typically overestimated T_2 values, both MANTIS and MANTIS-GAN had a similar unbiased estimation of T_2 values ($p>0.05$). For both cartilage subsections and meniscus, they achieved a more considerable agreement with the reference T_2 values, as indicated by the narrower limits of agreement lines (i.e., the dashed lines).

DISCUSSION & CONCLUSIONS

In this study, a deep learning-based reconstruction framework called MANTIS-GAN was proposed for rapid and efficient MR parameter mapping and was evaluated for T_2 mapping in the brain and the knee joint. Building on the foundation of MANTIS, the newly proposed MANTIS-GAN with adversarial learning not only maintained the original features of MANTIS but also enhanced the CNN mapping performance by enforcing a generation of high-quality parameter maps with image texture and sharpness preservation at a high acceleration rate.

Adversarial learning has proven to be effective in preserving perceptual image texture and sharpness in reconstructed images, as previously shown in (15,17,18) for static MR image reconstruction. While the pure pixel-wise losses such as l_1/l_2 norm and the hybrid of l_1/l_2 norm have been widely applied for many imaging studies, these simple loss functions aim to suppress the image noise and artifacts but can sometimes inevitably sacrifice image details and sharpness (13). The reconstructed images may alter the underlying image texture and the noise spectrum thus can result in the variation of image information. The reconstructed images using adversarial loss is more advantageous for maintaining image textures and patterns that present visually favorable appearance. Mathematically, successful convergence of the adversarial training can guarantee that the restored images and the training references fall into the same data distribution in a transformed high dimensional manifold (37,38). As shown in this study, adversarial learning can be directly extended and applied to the domain

of parameter maps to enforce the accurate image-to-parameter domain transform, meanwhile maintaining favorable preservation to image details. In both brain and knee applications, the perseveration of tissue structure can be important in delineating and evaluating small lesions and subtle tissue abnormalities caused by early pathologies, which otherwise could be missed due to image blurring.

Adversarial learning is also known to be challenging to train as the competitive nature of the CNN mapping (G) and CNN discriminator (D) can cause the learning process to be unstable(39). The resulted generation of image hallucinations (i.e., pseudo image structure) is malignant for image diagnosis. The MANTIS-GAN alleviates this concern by implementing the data consistency enforcement so that data fidelity loss (loss 1) can prevent degradation of the adversarial process from generating hallucinated features in parameter maps. The combination of all loss components in MANTIS-GAN is important as it imposes not only the efficient and rapid image feature learning but also the information consistency to provide robust end-to-end CNN mapping. It should also be noted that the optimization of the loss weights warrants further investigation. As the weight setting differs for different image datasets in our study via the grid search, it is highly likely that the optimal weights are dependent on the aspects of the training hyperparameters, such as the network architecture and the training datasets. In contrast to the manual and brute-force method for tuning loss weights, which can be tedious, time-consuming, and less repeatable. The recent proposed deep hyperparameter learning may provide a convenient solution by treating the loss weights as extra learnable variables and dynamically adjust them during the network training(40). Moreover, the adversarial learning can be further stabilized and improved by investigating several recent GAN architectures such as Wasserstein GAN (WGAN) (39), WGAN with Gradient Penalty (WGAN-GP) (41), Least Square GAN (LS-GAN) (42), and Deep Regret Analytic GAN (DRAGAN) (43), all of which are proven to improve the adversarial process.

There are several limitations in the current proof-of-concept study. Firstly, the MANTIS-GAN used the DICOM images after coil combination despite training CNN can be better using multi-coil *k*-space data. Similar to our previous deep learning reconstruction work for static MR images in Ref. (15), the extension of MANTIS-GAN for multi-coil data is entirely possible given access to the adequate multi-coil datasets and advanced GPU devices with more GPU memory. In addition, there are no limits for our method to reconstruct other undersampling trajectories. The MANTIS-GAN framework can also be extended to process non-Cartesian data such as spiral and radial by incorporating gridding and regridding operations and a density compensation function in the training process, similar to that in standard iterative non-Cartesian reconstruction. Secondly, the feasibility study of T2 mapping used a mono-exponential decay model for reconstructing multi-echo spin-echo images. Although this simple model might be suboptimal for this sequence due to the effects of stimulated echoes, non-ideal slice selection (44,45), it is expected that further improvement can be realized by using optimized imaging protocols and more advanced signal models, such as using the Bloch-simulation-based model to produce more reliable T_2 parameter estimations (45). Thirdly, adversarial learning in our study was applied to the full-scale image. While this implementation is preferable for anatomies such as white and gray matters in the brain with comparable size and spatial distribution, in another application such as knee joint, the sizeable structures, including bone and muscle, could dominate GAN

effort. Therefore, balanced optimization might be achieved through providing more attention to cartilage and meniscus in the knee to balance GAN effect in new GAN strategies. Finally, the research is warranted to investigate how and to what extent that MANTIS-GAN can be generalized to various imaging protocols and MR scanning environments for robust and reliable parameter mapping. For example, further studies are needed to investigate the generalization and robustness of the trained models at the presence of imaging protocol discrepancy between training and testing datasets. Future studies are also needed to validate the tolerance of MANTIS-GAN on image noise at a wide range of SNR levels.

In conclusion, we have demonstrated that the proposed MANTIS-GAN framework by synergistically incorporating the end-to-end CNN mapping, model enforced data consistency, and adversarial learning represents a promising deep learning approach for realizing efficient, rapid and high-quality MR parameter mapping.

ACKNOWLAGEMENT

REFERENCES

1. Margaret Cheng HL, Stikov N, Ghugre NR, Wright GA. Practical medical applications of quantitative MR relaxometry. J. Magn. Reson. Imaging 2012;36:805–824 doi: 10.1002/jmri.23718. [PubMed: 22987758]

2. Hammernik K, Klatzer T, Kobler E, et al. Learning a Variational Network for Reconstruction of Accelerated MRI Data. Magn. Reson. Med 2017;79:3055–3071 doi: 10.1002/mrm.26977. [PubMed: 29115689]

3. Wang S, Su Z, Ying L, et al. Accelerating Magnetic Resonance Imaging Via Deep Learning In: 2016 IEEE 13th International Symposium on Biomedical Imaging (ISBI). IEEE; 2016 pp. 514–517. doi: 10.1109/ISBI.2016.7493320.

4. Schlemper J, Caballero J, Hajnal JV., Price A, Rueckert D. A Deep Cascade of Convolutional Neural Networks for Dynamic MR Image Reconstruction. IEEE Trans. Med. Imaging 2017:1–1 doi: 10.1007/978-3-319-59050-9_51.

5. Han Y, Yoo J, Kim HH, Shin HJ, Sung K, Ye JC. Deep learning with domain adaptation for accelerated projection-reconstruction MR. Magn. Reson. Med 2018;80:1189–1205 doi: 10.1002/mrm.27106. [PubMed: 29399869]

6. Eo T, Jun Y, Kim T, Jang J, Lee HJ, Hwang D. KIKI-net: Cross-domain convolutional neural networks for reconstructing undersampled magnetic resonance images. Magn. Reson. Med 2018;80:2188–2201 doi: 10.1002/mrm.27201. [PubMed: 29624729]

7. Zhu B, Liu JZ, Cauley SF, Rosen BR, Rosen MS. Image reconstruction by domain-transform manifold learning. Nature 2018;555:487–492 doi: 10.1038/nature25988. [PubMed: 29565357]

8. Akçakaya M, Moeller S, Weingärtner S, U urbil K. Scan-specific robust artificial-neural-networks for k-space interpolation (RAKI) reconstruction: Database-free deep learning for fast imaging. Magn. Reson. Med 2019;81:439–453 doi: 10.1002/mrm.27420. [PubMed: 30277269]

9. Biswas S, Aggarwal HK, Jacob M. Dynamic MRI using model-based deep learning and SToRM priors: MoDL-SToRM. Magn. Reson. Med 2019 doi: 10.1002/mrm.27706.

10. Malavé MO, Baron CA, Koundinyan SP, et al. Reconstruction of undersampled 3D non-Cartesian image-based navigators for coronary MRA using an unrolled deep learning model. Magn. Reson. Med 2020;84:800–812 doi: 10.1002/mrm.28177. [PubMed: 32011021]

11. Liu F, Feng L, Kijowski R. MANTIS: Model-Augmented Neural neTwork with Incoherent k-space Sampling for efficient MR parameter mapping. Magn. Reson. Med 2019;82:174–188 doi: 10.1002/mrm.27707. [PubMed: 30860285]

12. Ronneberger O, Fischer P, Brox T. U-Net: Convolutional Networks for Biomedical Image Segmentation In: Navab N, Hornegger J, Wells WM, Frangi AF, editors. Medical Image Computing and Computer-Assisted Intervention -- MICCAI 2015: 18th International Conference, Munich, Germany, October 5–9, 2015, Proceedings, Part III. Cham: Springer International Publishing; 2015 pp. 234–241. doi: 10.1007/978-3-319-24574-4_28.

13. Zhao H, Gallo O, Frosio I, Kautz J. Loss Functions for Image Restoration With Neural Networks. IEEE Trans. Comput. Imaging 2017;3:47–57 doi: 10.1109/TCI.2016.2644865.

14. Goodfellow IJ, Pouget-Abadie J, Mirza M, et al. Generative Adversarial Networks. ArXiv e-prints 2014.

15. Liu F, Samsonov A, Chen L, Kijowski R, Feng L. SANTIS: Sampling-Augmented Neural neTwork with Incoherent Structure for MR image reconstruction. Magn. Reson. Med 2019;82:1890–1904 doi: 10.1002/mrm.27827. [PubMed: 31166049]

16. Liu F, Feng L. Towards High-Performance Rapid Quantitative Imaging via Model-based Deep Adversarial Learning. In: ISMRM Workshop on Data Sampling & Image Reconstruction.; 2020.

17. Quan TM, Nguyen-Duc T, Jeong W-K. Compressed Sensing MRI Reconstruction using a Generative Adversarial Network with a Cyclic Loss. IEEE Trans. Med. Imaging 2017;37:1488–1497 doi: 10.1109/TMI.2018.2820120.

18. Mardani M, Gong E, Cheng JY, et al. Deep Generative Adversarial Neural Networks for Compressive Sensing (GANCS) MRI. IEEE Trans. Med. Imaging 2018:1–1 doi: 10.1109/TMI.2018.2858752. [PubMed: 28945591]

19. Pruessmann Klaas P.,. Advances in Sensitivity Encoding With Arbitrary\nk-Space Trajectories. 2001;651:638–651.

20. Aubert-Broche B, Griffin M, Pike GB, Evans AC, Collins DL. Twenty new digital brain phantoms for creation of validation image data bases. IEEE Trans. Med. Imaging 2006;25:1410–1416 doi: 10.1109/TMI.2006.883453. [PubMed: 17117770]

21. Stanisz GJ, Odrobina EE, Pun J, et al. T1, T2 relaxation and magnetization transfer in tissue at 3T. Magn Reson Med 2005;54:507–512 doi: 10.1002/mrm.20605. [PubMed: 16086319]

22. Brown RW, Cheng YCN, Haacke EM, Thompson MR, Venkatesan R. Magnetic Resonance Imaging: Physical Principles and Sequence Design: Second Edition. (Brown RW, Cheng Y-CN, Haacke EM, Thompson MR, Venkatesan R, editors.) Chichester, UK: Wiley Blackwell; 2014. doi: 10.1002/9781118633953.

23. Liu F, Velikina JV., Block WF, Kijowski R, Samsonov AA. Fast Realistic MRI Simulations Based on Generalized Multi-Pool Exchange Tissue Model. IEEE Trans. Med. Imaging 2017;36:527–537 doi: 10.1109/TMI.2016.2620961. [PubMed: 28113746]

24. Bittoun J, Taquin J, Sauzade M. A computer algorithm for the simulation of any nuclear magnetic resonance (NMR) imaging method. Magn Reson Imaging 1984;2:113–120. [PubMed: 6530920]

25. Benoit-Cattin H, Collewet G, Belaroussi B, Saint-Jalmes H, Odet C. The SIMRI project: a versatile and interactive MRI simulator. J. Magn. Reson 2005;173:97–115 doi: 10.1016/j.jmr.2004.09.027. [PubMed: 15705518]

26. Lustig M, Donoho D, Pauly JM. Sparse MRI: The application of compressed sensing for rapid MR imaging. Magn Reson Med 2007;58:1182–1195 doi: 10.1002/mrm.21391. [PubMed: 17969013]

27. Isola P, Zhu J-Y, Zhou T, Efros AA. Image-to-Image Translation with Conditional Adversarial Networks. ArXiv e-prints 2016.

28. Chollet François. Keras. GitHub Published 2015.

29. Abadi M, Agarwal A, Barham P, et al. TensorFlow: Large-Scale Machine Learning on Heterogeneous Distributed Systems. ArXiv e-prints 2016 doi: 10.1109/TIP.2003.819861.

30. He K, Zhang X, Ren S, Sun J. Delving Deep into Rectifiers: Surpassing Human-Level Performance on ImageNet Classification. ArXiv e-prints 2015;1502.

31. Kingma DP, Ba J. Adam: A Method for Stochastic Optimization. ArXiv e-prints 2014.

32. Zhang T, Pauly JM, Levesque IR. Accelerating parameter mapping with a locally low rank constraint. Magn. Reson. Med 2015;73:655–661 doi: 10.1002/mrm.25161. [PubMed: 24500817]

33. Lingala SG, Hu Y, DiBella E, Jacob M. Accelerated Dynamic MRI Exploiting Sparsity and Low-Rank Structure: k-t SLR. IEEE Trans. Med. Imaging 2011;30:1042–1054 doi: 10.1109/TMI.2010.2100850. [PubMed: 21292593]

34. Krotkov EP. Active Computer Vision by Cooperative Focus and Stereo. New York, NY: Springer New York; 1989. doi: 10.1007/978-1-4613-9663-5.

35. Buerkle A, Schmoeckel F, Kiefer M, et al. Vision-based closed-loop control of mobile microrobots for microhandling tasks In: Nelson BJ, Breguet J-M, editors. Microrobotics and Microassembly III. Vol. 4568 SPIE; 2001 p. 187. doi: 10.1117/12.444125.

36. Giavarina D Understanding Bland Altman analysis. Biochem. Medica 2015;25:141–151 doi: 10.11613/BM.2015.015.

37. Green B, Horel T, Papachristos AV. Modeling Contagion Through Social Networks to Explain and Predict Gunshot Violence in Chicago, 2006 to 2014. JAMA Intern. Med 2017;177:326 doi: 10.1001/jamainternmed.2016.8245. [PubMed: 28055070]

38. Ye JC, Han Y, Cha E. Deep Convolutional Framelets: A General Deep Learning Framework for Inverse Problems. ArXiv e-prints 2017.

39. Arjovsky M, Chintala S, Bottou L. Wasserstein GAN. 2017.

40. Cipolla R, Gal Y, Kendall A. Multi-task Learning Using Uncertainty to Weigh Losses for Scene Geometry and Semantics. Proc. IEEE Comput. Soc. Conf. Comput. Vis. Pattern Recognit 2018:7482–7491 doi: 10.1109/CVPR.2018.00781.

41. Gulrajani I, Ahmed F, Arjovsky M, Dumoulin V, Courville A. Improved Training of Wasserstein GANs. ArXiv e-prints 2017.

42. Mao X, Li Q, Xie H, Lau RYK, Wang Z, Smolley SP. Least Squares Generative Adversarial Networks. ArXiv e-prints 2016.

43. Kodali N, Abernethy J, Hays J, Kira Z. On Convergence and Stability of GANs. ArXiv e-prints 2017.

44. Hennig J Multiecho imaging sequences with low refocusing flip angles. J. Magn. Reson 1988;78:397–407 doi: 10.1016/0022-2364(88)90128-X.

45. Ben-Eliezer N, Sodickson DK, Block KT. Rapid and accurate T2 mapping from multi-spin-echo data using bloch-simulation-based reconstruction. Magn. Reson. Med 2015;73:809–817 doi: 10.1002/mrm.25156. [PubMed: 24648387]
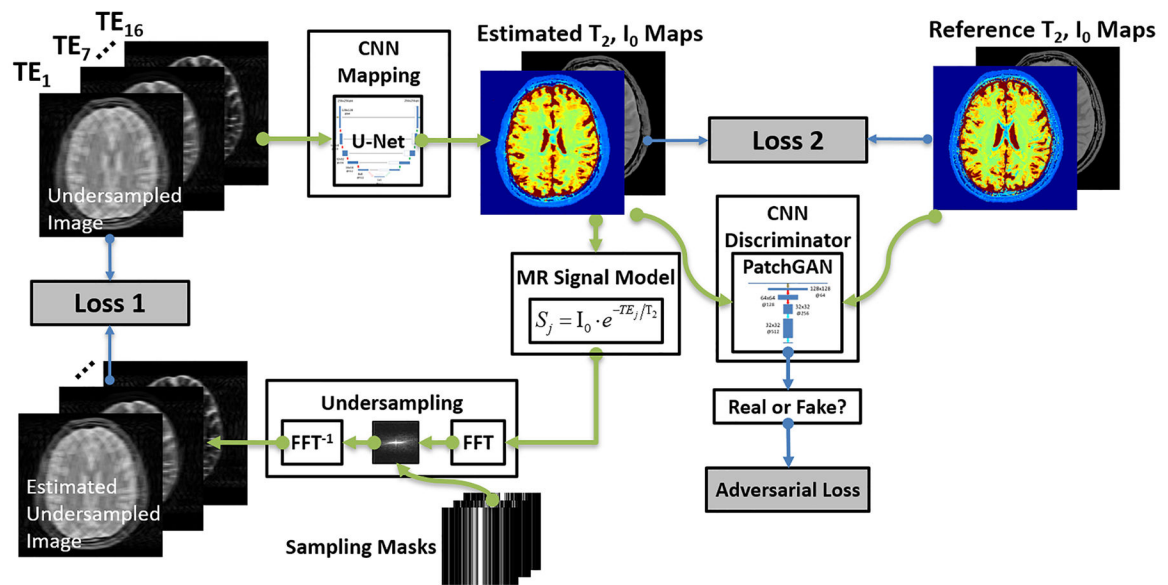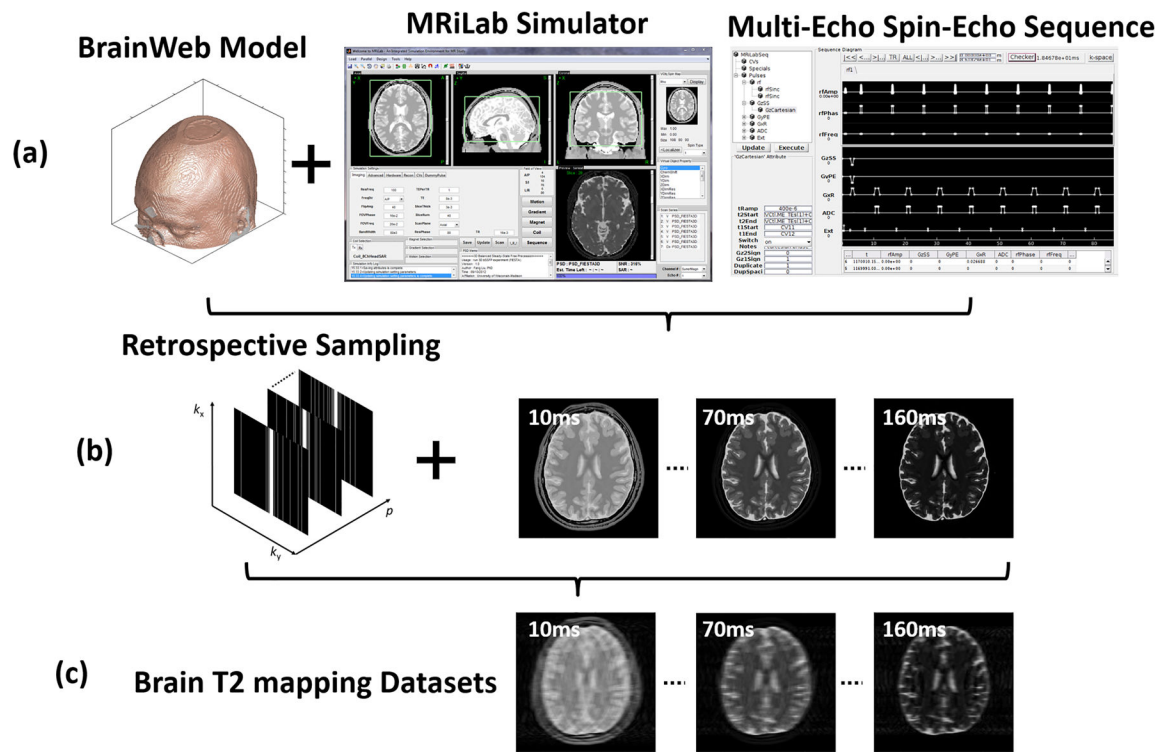
Figure 1:
The schematic demonstration of the MANTIS-GAN framework. The MANTIS framework uses two components, including the first loss term (loss 1) to enforce data consistency between the synthetic undersampled data and the acquired k-space measurements; and the second loss term (loss 2) to ensure the similarity between the estimated parameter maps and the reference parameter maps. Building on the foundation of this framework, MANTIS-GAN introduces the third adversarial loss highlighting that estimated maps resemble the same tissue features and image sharpness as the reference maps from fully sampled data. The MANTIS-GAN framework synergizes the data-driven and MR physics-informed knowledge and introduces adversarial training for improved detail preservation.

Figure 2:

The schematic demonstration for the simulated brain image datasets. **(a)** One of 20 McGill BrainWeb phantoms applied to generate realistic brain MR datasets using the MRiLab simulator and a multi-echo spin-echo sequence for T_2 mapping at 1.5T. **(b)** 1D Cartesian variable-density undersampling masks used for 16 echoes. **(c)** The generated undersampled T_2 mapping images for evaluating deep learning-based reconstruction algorithms.
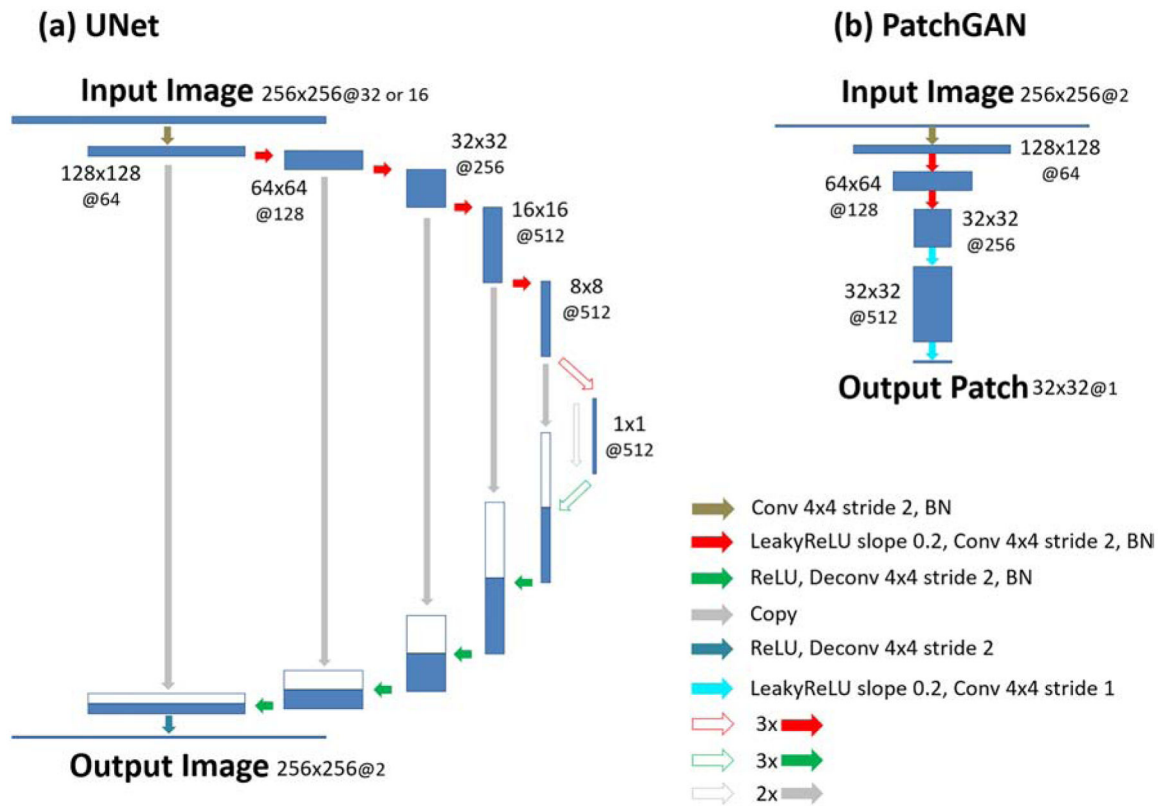
Figure 3:
The configuration of U-Net and PatchGAN in MANTIS-GAN for end-to-end CNN mapping and adversarial training. The U-Net consists of a paired encoder and decoder network. Several shortcut connections were used to transfer image features directly between encoder and decoder to enhance the mapping performance. The configuration of the convolution layers is shown as image size @ the total number of 2D filters. Abbreviation includes BN: Batch Normalization; ReLU: Rectified Linear Unit activation; Conv: 2D convolution; Deconv: 2D deconvolution
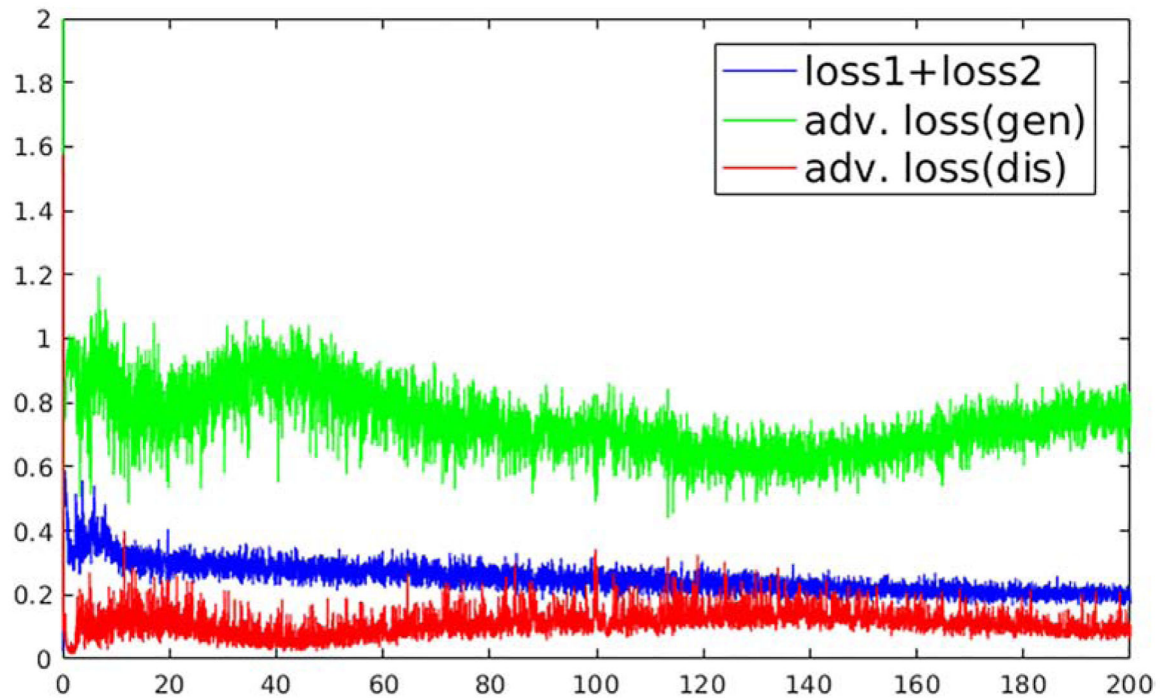
Figure 4:
The overall losses as a function of the training process at each epoch for training MANTIS-GAN on the brain image datasets. The image loss (loss 1 + loss 2) decreases during the training and converges into stable status after 180 epochs. The adversarial training demonstrates a competing form of adversarial loss behavior for generator (U-Net) and discriminator (PatchGAN) (without the logarithm for display purposes). The adversarial training creates a mechanism to mutually improve generator and discriminator to improve the final reconstruction output.
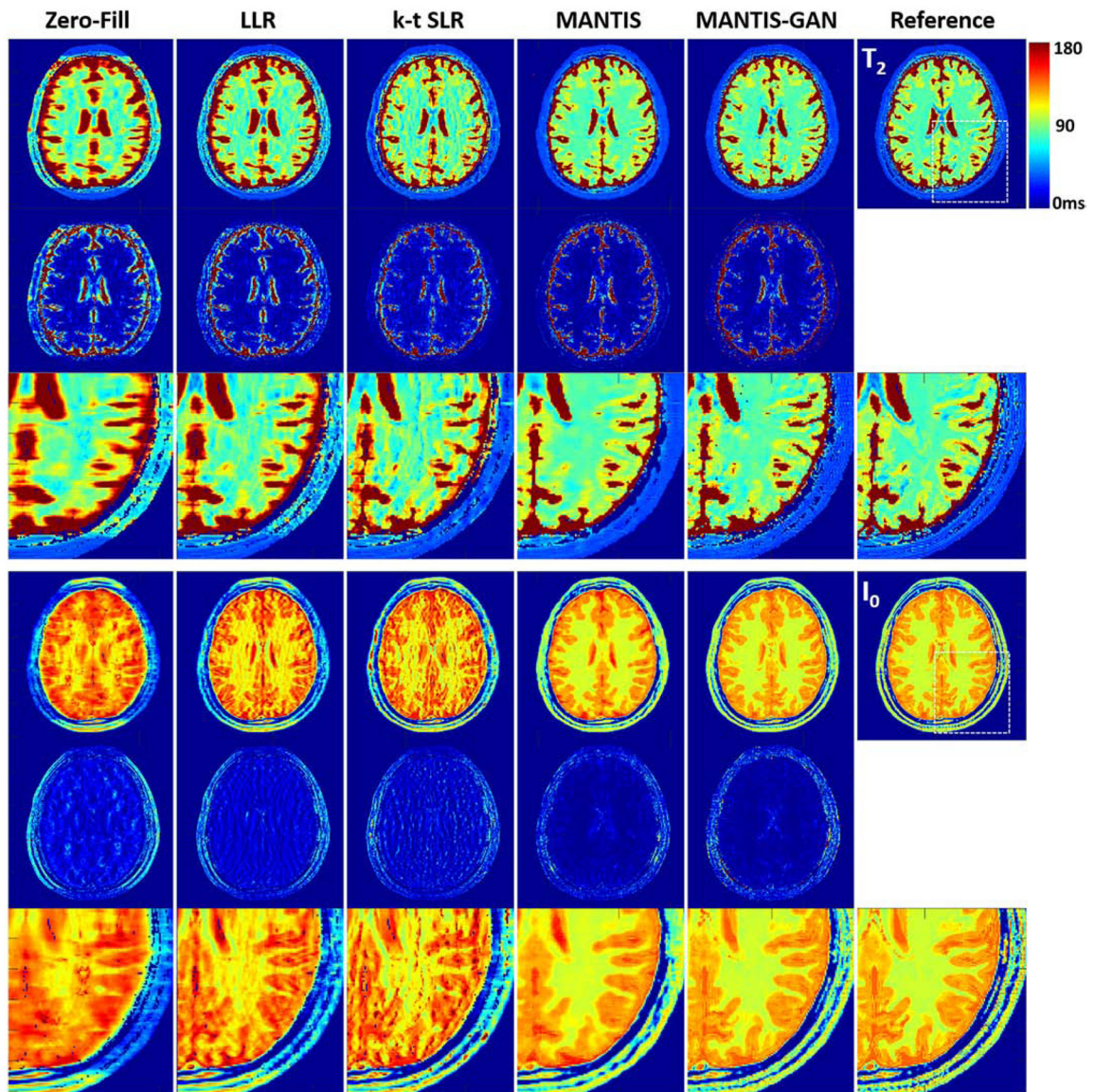
Figure 5:

Comparison of T_2 and I_0 maps reconstructed from MANTIS-GAN and MANTIS with maps from joint x-p reconstruction methods at an acceleration rate R=8 in one simulated axial brain slice. The difference maps under the reconstructed T_2 and I_0 maps show the absolute pixel-wise error at the same color scale. MANTIS removed most of the image artifact but resulted in image blurring at the tissue boundaries. MANTIS-GAN generated nearly artifact-free T_2 and I_0 maps with well-preserved image sharpness, clarity, and tissue texture like the reference maps. The joint x-p reconstruction methods resulted in parameter maps at reduced image sharpness and remaining residual artifacts.
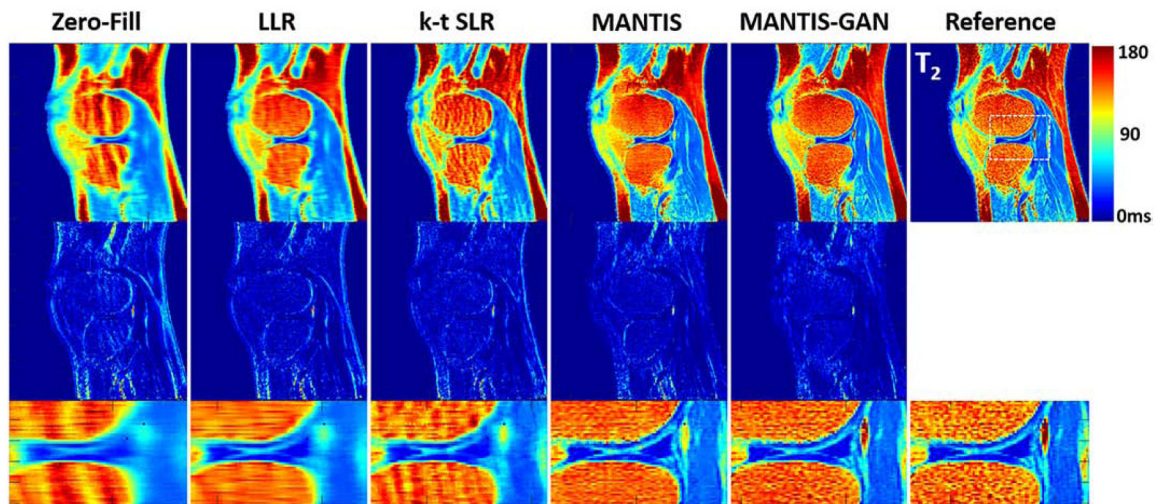
Figure 6:
Comparison of T_2 maps reconstructed from MANTIS-GAN and MANTIS with maps from joint x-p reconstruction methods at an acceleration rate R=8 in one real sagittal knee slice. The difference maps under the reconstructed T_2 maps show the absolute pixel-wise error at the same color scale. MANTIS and MANTIS-GAN removed most of the image artifact, and MANTIS-GAN generated better bone texture and sharper image appearance that is comparable to the reference maps. Other methods cannot remove the residual artifacts caused by the high undersampling rate.
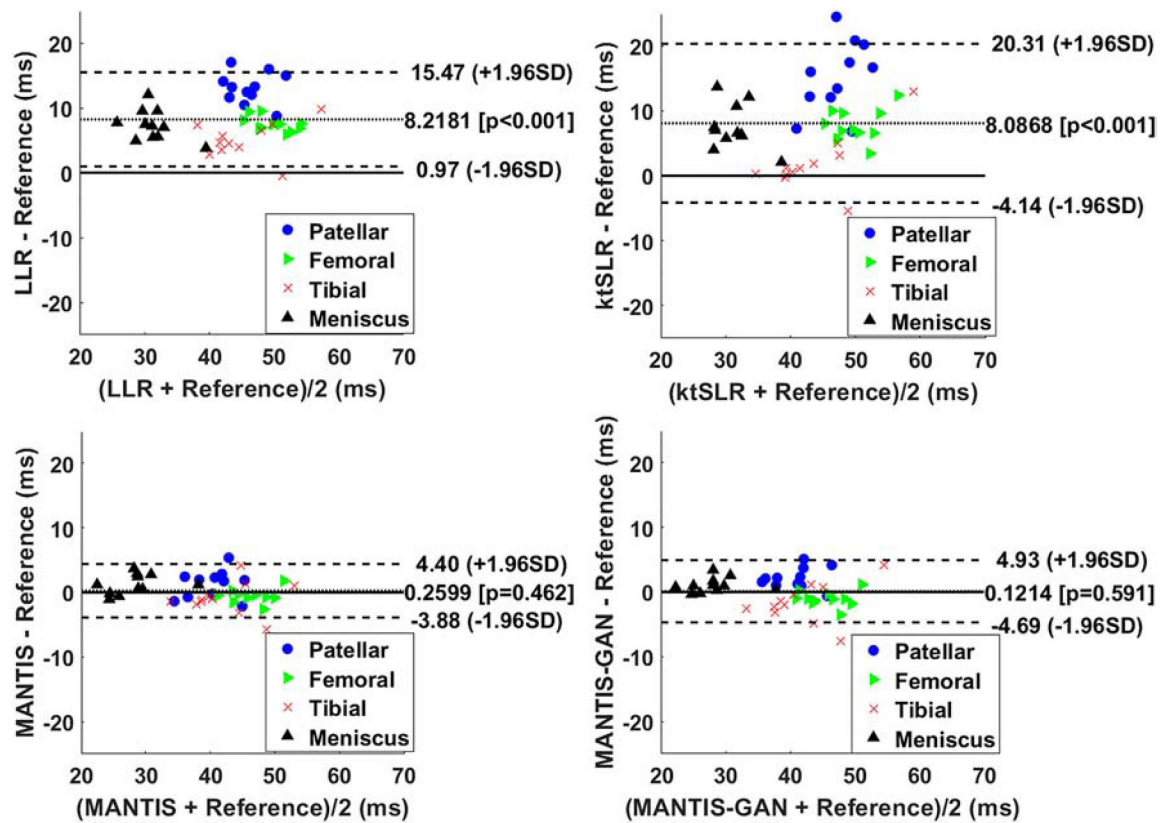
Figure 7:

The Bland-Altman plots for the agreement of the regional cartilage and meniscus T_2 values in the testing knee datasets between the reference and the T_2 maps reconstructed from different methods at an acceleration rate R=8. MANTIS and MANTIS-GAN achieved unbiased estimation (p>0.05) of the T2 values for cartilage and meniscus with narrower limits of agreements (the dashed lines), which are calculated at the ±1.96*standard deviation of the mean differences.

Table 1:

The mean and standard deviation (SD) of nRMSE, SSIM, and Tenengrad measures on testing datasets for brain and knee joint, respectively. MANTIS-GAN achieved the reconstruction performance with the highest image sharpness (i.e., lowest Tenengrad measures) and best texture preservation (i.e., highest SSIM measures) in contrast to the reference. MANTIS achieved the greatest noise suppression (i.e., lowest nRMSE measures).

Methods	Mean ± SD at Brain Datasets			Mean ± SD at Knee Datasets		
	nRMSE (%)	SSIM (%)	Tenengrad (%)	nRMSE (%)	SSIM (%)	Tenengrad (%)
LLR	10.9 ± 4.2	50.2 ± 5.3	35.4 ± 6.3	13.7 ± 3.4	58.2 ± 3.1	41.7 ± 8.3
k-t SLR	6.8 ± 2.5	66.5 ± 3.4	20.6 ± 4.3	11.4 ± 2.5	69.8 ± 3.5	19.1 ± 2.2
MANTIS	**3.4 ± 1.8**	83.1 ± 1.9	15.6 ± 3.9	**7.1 ± 1.9**	81.1 ± 2.1	11.6 ± 3.1
MANTIS-GAN	3.6 ± 2.1	**85.1 ± 2.6**	**9.2 ± 3.2**	7.3 ± 2.2	**83.2 ± 2.4**	**10.1 ± 2.3**